Key Engineering Materials
ISSN: 1662-9795, Vol. 1047, pp 127-137

Submitted: 2026-01-16
Revised: 2026-02-25
Accepted: 2026-02-25
Online: 2026-04-13

Effect of Hatch Distance and Scanning Speed Combinations at Constant Volumetric Energy Density on the Materials Properties of IN939 Fabricated by Powder Bed Fusion–Laser Beam

Merve Nur Doğu[1,2,a*], Meris Meric Ikiz[1,2,b], Gavin Chapman[1,2,c], Sampreet Rangaswamy[1,2,d], Merve Yesim Yalcin[3,4,e], Seren Ozer[5,6,f], Kemal Davut[7,g] and Dermot Brabazon[1,2,h]

[1]I-Form Advanced Manufacturing Research Centre, Dublin City University, Dublin, Ireland

[2]DCU Institute for Advanced Processing Technology, School of Mechanical & Manufacturing Engineering, Dublin City University, Dublin, Ireland

[3]I-Form Advanced Manufacturing Research Centre, University College Dublin, Dublin, Ireland

[4]School of Mechanical and Materials Engineering, University College Dublin, Dublin, Ireland

[5]Department of Metallurgical and Materials Engineering, Atılım University, Ankara, Türkiye

[6]Department of Metallurgical and Materials Engineering, Middle East Technical University, Ankara, Türkiye

[7]Department of Materials Science and Engineering, Izmir Institute of Technology, 35430, Urla, Izmir, Türkiye

[a*]mervenur.dogu@dcu.ie, [b]meris.ikiz2@mail.dcu.ie, [c]gavin.chapman3@mail.dcu.ie, [d]sampreet.rangaswamy2@mail.dcu.ie, [e]merve.yalcin@ucdconnect.ie, [f]ozer.seren@metu.edu.tr, [g]kemaldavut@iyte.edu.tr, [h]dermot.brabazon@dcu.ie

[*]corresponding author: mervenur.dogu@dcu.ie

Keywords: powder bed fusion–laser beam, IN939, volumetric energy density, relative density, defect formation, microstructure, surface roughness, infra-red (IR).

Abstract. This study provides a comprehensive investigation into the effects of different scanning parameter combinations-specifically scanning speed and hatch distance-on the material properties of IN939 fabricated using the powder bed fusion-laser beam (PBF-LB) process under a constant volumetric energy density (VED). Despite the fixed VED, the fabricated samples experienced different thermal cycles, resulting in distinct microstructural features and corresponding variations in material performance. In-situ infrared monitoring indicated that the sample with the narrowest hatch distance and highest scanning speed (Sample 1) reached the highest normalized temperatures with intense heat accumulation, whereas wider hatch distances (Sample 3) promoted lower and more stable temperature distributions. The results revealed that the intermediate parameter set (Sample 2) achieved the highest relative density (99.29%) and the lowest surface roughness. In contrast, both the narrowest and widest hatch spacing combinations promoted increased porosity, primarily consisting of lack-of-fusion (LoF) and gas pores. Electron backscatter diffraction (EBSD) analysis showed that the area-weighted average grain size increased from 29.5 μm to 36.7 μm as the hatch distance increased. Texture analysis indicated generally weak crystallographic texture development, with only slight intensification of <001>//BD and <111>//BD components, attributed to the 67° rotation strategy. Furthermore, the microhardness values demonstrated negligible variation across the samples, ranging from 356.7 ± 14.3 HV1 to 360.1 ± 10.5 HV1. This limited variation indicates that the strengthening behavior was predominantly governed by the combined influence of defect density and matrix–defect interactions, rather than being directly correlated with grain size.

1. Introduction

In PBF-LB, the components are produced by selectively melting powder particles in a layer-wise manner, following digital geometries defined by computer-aided design (CAD) data and thereby allows reducing dependence on assembly operations and minimizing defect formation associated with secondary processing steps [1]. Additional advantages of PBF-LB include high dimensional accuracy, the potential for weight reduction through the fabrication of lattice or cellular structures, and a significant decrease in material waste and overall production costs [2].

IN939 is a precipitation-strengthened Ni-based superalloy in which mechanical strength is predominantly achieved through the formation of $L1_2$-ordered γ′ ($Ni_3(Al,Ti)$) precipitates [3]. IN939 is typically developed for service conditions up to approximately 850 °C, particularly in gas turbine applications, and is characterized by high mechanical strength together with excellent corrosion and oxidation resistance [4,5]. However, process-inherent defects—including gas pores, keyhole- and lack of fusion (LoF)-related pores, and particularly cracking—may arise during fabrication. These defects are primarily associated with the high Al and Ti contents, which impair weldability and are further intensified by the rapid solidification behaviour characteristic of the PBF-LB process [6–8].

The thermal behaviour characteristic of the PBF-LB process is governed by a highly coupled set of physical phenomena, including laser-powder interaction, high thermal gradients, localized melting and rapid solidification of powder particles. The resulting microstructural features and the quality of the produced components are strongly dependent on critical process variables such as laser power (P), scanning speed (v), hatch distance (h), and layer thickness (t). In combination, these parameters determine the VED (Eq. (1)), which represents the energy input per unit volume of the powder bed [9,10].

$$\mathrm{VED} = \frac{\mathrm{P}}{\mathrm{v.\ h.t}} \quad (J/mm^3) \tag{1}$$

It is known that the optimization of VED parameters is critical and must be systematically tailored to the material and application requirements in order to ensure complete densification, reduced surface roughness, and improved mechanical performance. Nevertheless, systematic investigations focusing on the optimization and influence of VED in PBF-LB-processed IN939 remain limited in the existing literature. In our previous study [11], the influence of various process parameters that govern the VED was systematically examined with respect to relative density, microstructural evolution, defect formation (i.e., porosity and cracking), and surface-related characteristics. The results revealed that, although arc-shaped melt pools were observed under all processing conditions, samples fabricated at high VED exhibited pronounced irregularly shaped pores and the presence of micro-cracks. Moreover, increasing the hatch spacing from 50 µm to 110 µm resulted in a reduction in the surface roughness of the produced samples. Marchese et al. [12] varied the VED from 30 to 320 J mm^{-3} to investigate its influence on the density and microstructural characteristics of PBF-LB-produced IN939. Their results demonstrated that both low VED (< 50 J mm^{-3}) and excessively high VED (> 160 J mm^{-3}) values promoted the formation of large-scale defects, with sizes reaching several hundred micrometers. These defects were attributed to the development of LoF defects under insufficient melting conditions and to keyhole-induced pores resulting from melt pool instability at elevated energy inputs. Dursun et al. [13] demonstrated that adjusting the VED within the range of 35–109 J mm^{-3} resulted in notable variations in melt pool morphology and relative density, with certain processing conditions also promoting the onset of the balling phenomenon.

Although several studies have been reported in literature, the majority primarily investigate the influence of varying VED values on material properties. In contrast, the effect of identical VED conditions has not yet been systematically explored, which is essential for isolating and clarifying the role of equivalent energy input. To address this gap, three sets of IN939 samples were fabricated using different combinations of scanning speed and hatch distance while maintaining the same VED. The samples were subsequently characterized in detail to assess surface roughness, relative density, and defect formation, along with microstructural features and microhardness.

2. Materials and Methodology

2.1. IN939 fabrication by the PBF-LB process

Gas-atomized powder (Truform 939-N65, Praxair Surface Technologies) with a particle size range of 17.4–52 µm were utilized for the production of the samples by PBF-LB. The powder chemical composition is listed in Table 1, and a comprehensive characterization of the feedstock powder has been reported previously by the authors [14].

Table 1. The nominal chemical composition (wt.%) of the gas-atomized IN939 powder.

Elements	Al	Co	Cr	Nb	Ta	Ti	W	Zr	Ni	B	C	O	N
wt.%	1.9	18.9	22.8	1.0	1.4	3.8	2.0	0.028	Bal.	0.004	0.16	0.014	0.009

IN939 samples were fabricated using an Aconity MINI (GmbH) laser-based metal additive manufacturing (AM) platform. All builds were performed under a protective argon atmosphere with a purity of 99.999%, while the oxygen level was controlled below 50 ppm to eliminate oxidation. CK45 steel served as the build plate material. Cubic specimens with dimensions of 10 × 10 × 10 mm³ were produced while maintaining a constant VED through systematic variation of scan speed and hatch distance. The PBF-LB processing conditions investigated in this study, together with the corresponding sample designations, are summarized in Table 2. The VED was calculated using Eq. (1).

The Aconity MINI has two coaxial infrared pyrometers (KLEIBER Infrared GmbH) for in-situ infrared (IR) monitoring of melt pool thermal emission. Due to the absence of material-specific temperature calibration for IN939, the melt pool response output was in relative units (mV) rather than absolute temperature values. The acquired data, mapped to the (x,y) coordinates of the build plate, were processed using Python. Melt pool thermal distributions were visualized using normalized thermograms, with statistical mean layer values scaled between 0 and 1 to represent relative temperature variations.

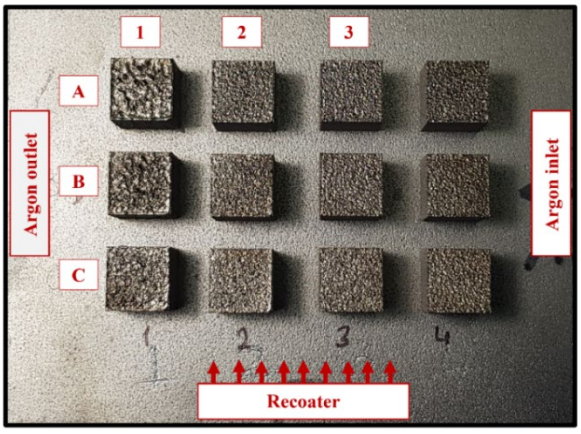

Fig. 1. Images of the build plate after fabrication of the as-built IN939 samples.

Table 2. PBF-LB process parameters used in the present study.

Sample		Hatch distance (µm)	Scanning speed (mm/s)	VED (J/mm³)	Power (W)	Layer thickness (µm)	Spot size (µm)	Scanning strategy
1	1A	40	1350	92.6	200	40	80	Alternating bi-directional scan with 67° rotation between the adjacent layers
	1B							
	1C							
2	2A	60	900					
	2B							
	2C							
3	3A	80	675					
	3B							
	3C							

2.2. Surface roughness measurements

Surface topography of the as-built samples was characterized using a Bruker ContourGT optical profilometer. Measurements were performed on the XY planes (perpendicular to the build direction) over an area of 5 × 5 mm². In addition, surface roughness was evaluated on XZ planes (parallel to the build direction) at both the argon inlet and outlet sides, using a scan area of 3 × 3 mm². Surface roughness was quantified using the areal parameter Sa, defined as the arithmetic mean height, while Sz was used to describe the sum of the maximum peak height and the maximum pit depth.

2.3. Relative density and porosity measurements

The relative density values of the as-built samples were determined using Archimedes' principle in accordance with ASTM B311-17 [15]. Measurements were performed with a Sartorius Entris II Essential BCE124I-1S analytical balance, offering an accuracy and repeatability of ±0.1 mg. Ethanol (Lenox, 99.99%) was employed as the immersion medium. For each sample, three independent measurements were performed, and the resulting values were averaged to determine the final relative density. A theoretical density of 8.15 g cm^{-3} was assumed for fully dense IN939 in the calculation of relative density.

Conventional optical microscopy was used to examine the spatial distribution of porosity in the as-built samples. Polished cross-sections from both the XZ and XY orientations were imaged using the stitching function of a Keyence 3D optical microscope to obtain large-area views. Porosity quantification was carried out by analyzing the stitched optical images with ImageJ software, comprising a minimum of 20 images for the XZ planes.

2.4. Microstructural characterization

The hot-mounted specimens were first subjected to automated grinding using conventional SiC abrasive papers up to 1200 grit, followed by polishing with progressively finer diamond suspensions (9, 3, and 1 μm) using a Struers Tegramin-20 system. For EBSD analysis, an additional electropolishing step was applied using a Struers Lectropol-5 unit with Struers A2 electrolyte at 40 V, a flow rate of 16, and a polishing duration of 15 s. For microstructural observation, selected samples were electrochemically etched after electopolishing with Struers A2 electrolyte at 5 V, a flow rate of 15, and an etching time of 5 s. Microstructural characterization was performed using a Keyence VHX2000E 3D digital optical microscope and a Zeiss EVO LS-15 scanning electron microscope (SEM). Electron backscatter diffraction (EBSD) measurements were carried out with an Oxford Symmetry S3 detector operated at an accelerating voltage of 20 kV and a probe current of 7.0 nA. Orientation maps covering an area of 350 × 350 μm² were acquired with a step size of 0.75 μm, and the raw EBSD data were post-processed using AZtecCrystal 3.3 software.

2.5. Microhardness

The Vickers microhardness of the as-built samples was evaluated on the XZ planes using a Zwick/Roell DuraScan G5 semi-automatic microhardness tester with an applied load of 1 kg, in accordance with ASTM E384 [16]. For each specimen, ten individual indentations were performed, and the reported hardness values represent the corresponding average.

3. Results and Discussion

3.1. In-situ temperature monitoring

Fig. 2 shows the normalized melt pool temperature data used to assess the thermal history during the PBF-LB process, highlighting the strong influence of laser processing parameters on heat accumulation. Sample 1 showed the highest and most unstable thermal response throughout the build, which is mainly associated with the combination of high scan speed and narrow hatch spacing [17]. The reduced hatch distance limited inter-track cooling, promoting localized heat buildup and an unstable melt pool, as further evidenced by the corresponding 2D and 3D thermal maps. In contrast,

Samples 2 and 3, fabricated with wider hatch distances, exhibited lower and more stable temperature distributions, indicating more effective thermal dissipation during processing.

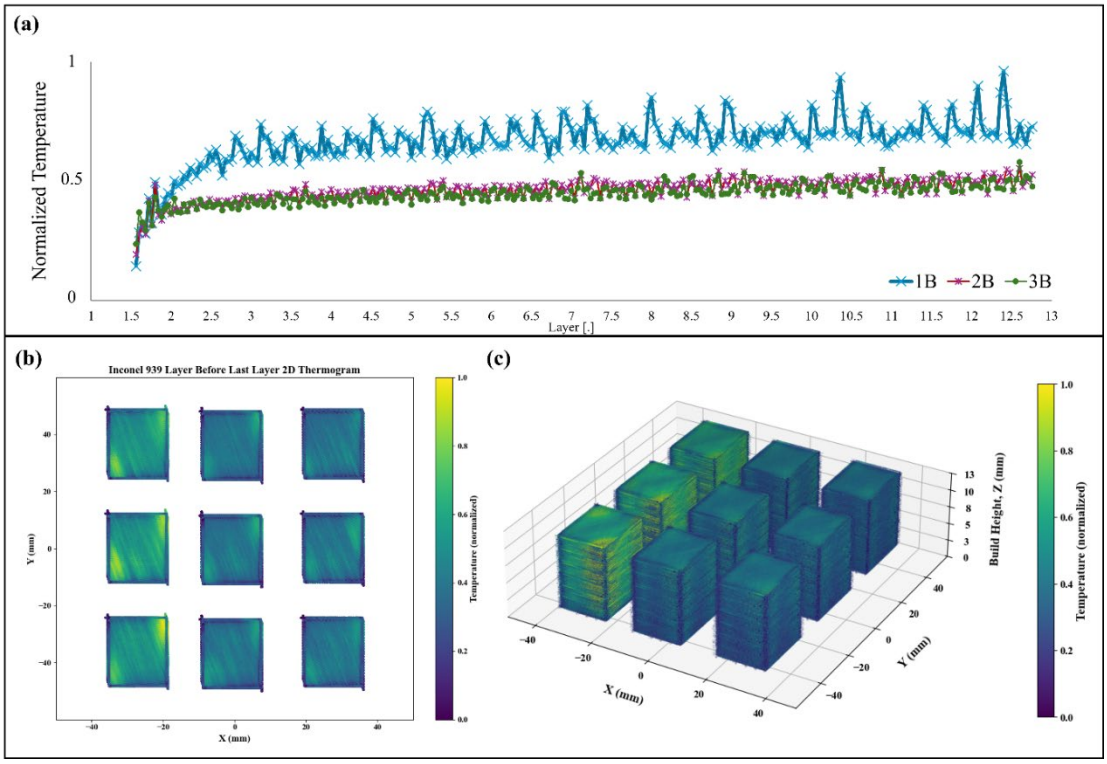

Fig. 2. Thermal analysis of IN939 samples during the build process: (a) Normalized mean temperature evolution across build layers for selected samples (1B, 2B, and 3B). (b) 2D thermogram of the second last layer, showing the temperature distribution across nine cubic samples. (c) 3D spatial visualization of the thermal data throughout the build height; the color bar indicates normalized temperature values.

3.2. Surface roughness

The corresponding Sa and Sz values, categorized by the XY and XZ planes and by different measurement locations, are summarized in Table 3. Surface roughness profiles of selected samples, together with bar charts illustrating the associated Sa and Sz values, are presented in Fig. 3. The results indicated that hatch distance and scanning speed have a pronounced influence on the average surface roughness of the as-built samples. Sample 1 exhibited the highest surface roughness in both the XY and XZ planes (Sa = 22.72 µm and 8.51 µm, respectively), which is consistent with the thermal instabilities identified in the infrared monitoring data. The combination of high scanning speed and narrow hatch distance promoted excessive track overlap and localized heat accumulation, resulting in an elevated and highly fluctuating thermal response. This excessive thermal input destabilized the melt pool, hindered uniform track consolidation, and led to pronounced surface irregularities, as confirmed by the corresponding 3D surface topography. In contrast, Sample 2 showed the lowest surface roughness, with Sa values of 13.95 µm in the XY plane and 6.29 µm in the XZ plane. This improvement is attributed to the use of an intermediate hatch spacing (60 µm) and a moderate scanning speed (900 mm/s), which promoted a more stable melting regime and reduced temperature fluctuations. These conditions resulted in improved surface uniformity and limited spatter-related surface defects. Although Sample 3 was processed at a lower scanning speed (675 mm/s), which increased the longer laser–material interaction time, its larger hatch spacing (80 µm) might have led to insufficient track overlap, resulting in poorer surface uniformity compared to Sample 2. Furthermore, the consistently higher roughness observed on XZ plane of the samples near the argon outlet suggests that gas flow behaviour and spatter accumulation further contribute to surface irregularities associated with thermal effects [18].

Table 3. Average surface roughness (Sa) and maximum height (Sz) values measured on the XY and XZ planes of the as-built IN939 samples.

Sample		Sa (μm)					
		XY plane		XZ plane (argon inlet)		XZ plane (argon outlet)	
1	1A	22.07	**22.72 ± 0.85**	8.82	**8.51 ± 0.60**	14.63	**15.08 ± 0.50**
	1B	23.68		8.89		15.62	
	1C	22.40		7.81		14.98	
2	2A	12.78	**13.95 ± 1.10**	6.71	**6.29 ± 0.39**	14.62	**12.91 ± 1.60**
	2B	14.96		6.20		12.66	
	2C	14.10		5.95		11.45	
3	3A	15.18	**17.19 ± 1.83**	6.16	**6.49 ± 0.60**	11.86	**12.45 ± 1.17**
	3B	18.77		7.18		13.80	
	3C	17.62		6.12		11.69	
Sample		**Sz (μm)**					
		XY plane		**XZ plane (argon inlet)**		**XZ plane (argon outlet)**	
1	1A	192.92	**191.13 ± 1.56**	175.61	**155.13 ± 17.79**	161.81	**158.63 ± 6.38**
	1B	190.42		146.18		162.80	
	1C	190.05		143.59		151.28	
2	2A	153.88	**167.62 ± 20.01**	132.33	**113.81 ± 17.03**	150.67	**163.67 ± 12.01**
	2B	158.39		98.83		174.35	
	2C	190.58		110.28		165.99	
3	3A	176.60	**186.79 ± 10.04**	140.53	**145.37 ± 4.33**	171.84	**173.89 ± 4.91**
	3B	196.67		146.73		179.50	
	3C	187.10		148.86		170.34	

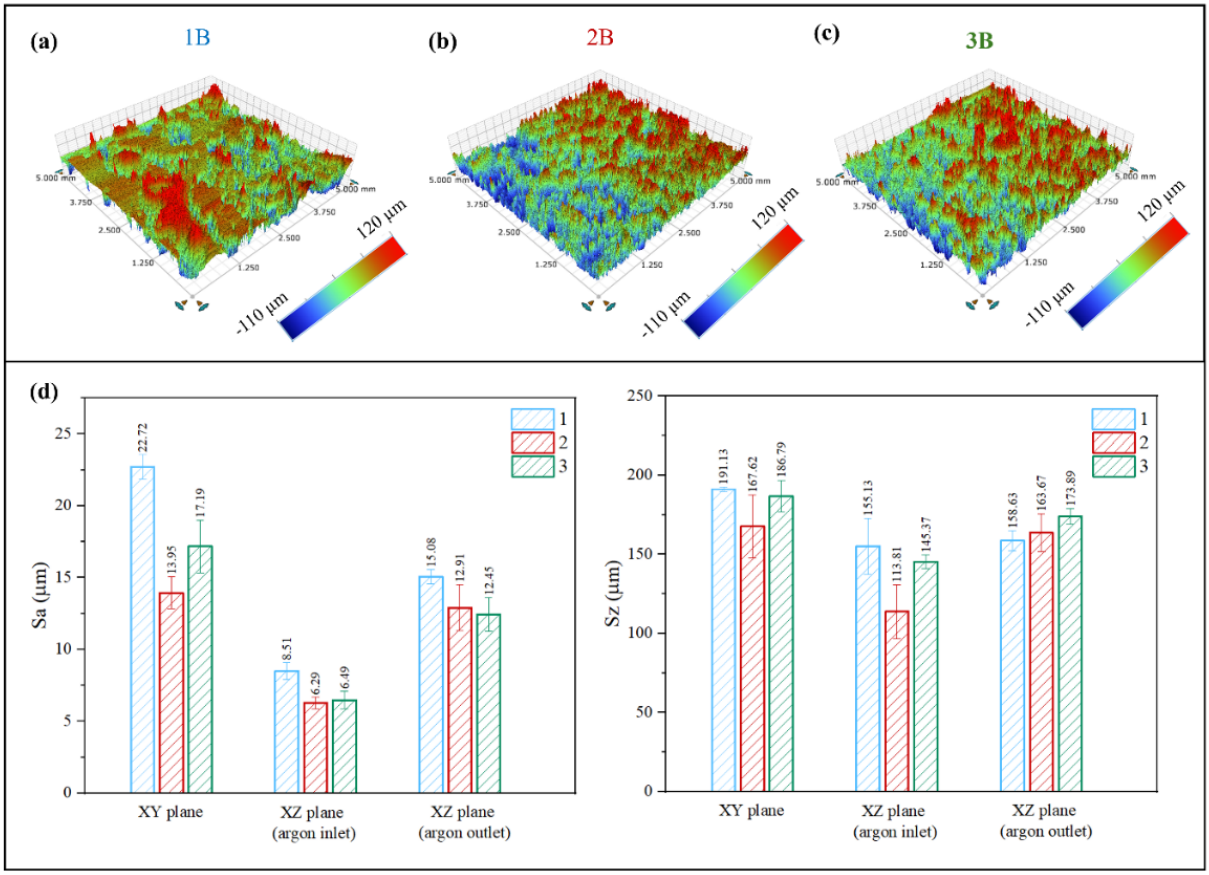

Fig. 3. (a–c) Surface roughness profiles of selected as-built IN939 samples (1B, 2B, and 3B), and (d) bar charts summarizing the average Sa and Sz values for the samples.

3.3. Relative density and defect formation

The average relative density of the samples was determined using the Archimedes method, while the average porosity percentage (%), pore density (pores/mm²), and average Feret size (µm) (as a quantitative measure of pore size) were quantified through ImageJ analysis. The corresponding results are summarized in Table 4. It should be noted that defect analysis was performed by accounting for all gas pores, LoF-related pores, and keyhole-induced pores identified on the as-polished surfaces, as also presented in Fig. 4. As given, the Sample 2 exhibited the highest average relative density of 99.29%, whereas the relative density values for Sample 1 and Sample 3 were comparable, measured as 98.65% and 98.75%, respectively. Consistent with the density measurements, Sample 2 exhibited the lowest average porosity percentage, pore density, and Feret size, measured as 0.05%, 5.09 pores/mm², and 11.09 µm, respectively. It is well established that the integrity and performance of additively manufactured components are strongly influenced by defect population; therefore, achieving high relative density in conjunction with a low defect content is generally associated with superior mechanical performance. Interestingly, although the pore density of these two samples fell within a narrow range of 6.14–6.45 pores/mm², Sample 3 exhibited a substantially lower average porosity percentage and Feret size compared to Sample 1, with values of 0.20% and 19.42 µm, respectively. Defect and microstructural analyses (Fig. 4) further revealed that Sample 1 contained very large, irregularly shaped pores with sizes reaching up to 1 mm, in agreement with its high average Feret diameter of 31.98 µm. In contrast, Sample 3 predominantly consisted of small, near-spherical pores with maximum sizes of approximately 60–70 µm, accompanied by only a limited number of large pores. It can be stated that the combination of a lower hatch distance (40 µm) and a high scanning speed (1350 mm/s) promoted the formation of a large number of defects, predominantly LoF-related pores, in Sample 1. Moreover, the use of a relatively large hatch distance (80 µm) during the fabrication of Sample 3 may have contributed to the development of some large LoF-related pores, due to insufficient inter-track overlap. However, most of the defects observed in Fig. 4(c) are small and spherical in shape, suggesting that gas porosity is the dominant defect type, while a smaller fraction may be associated with keyhole-related pore formation. Gas pore formation is primarily associated with entrapped gas, either within the feedstock powder particles introduced during the atomization process or trapped during the rapid solidification of the molten metal in the PBF-LB process [19]. On the other hand, keyhole-related porosity may arise under conditions of excessive energy input, wherein intense vaporization of the molten metal induces recoil pressure, resulting in keyhole instability and the entrapment of pores during solidification [19–21]. The use of a low scanning speed (675 mm/s) during the fabrication of Sample 3 may have promoted the formation of these defects within the microstructure by increasing local energy input.

Table 4. Image J porosity analysis and Archimedes-based relative density results of as-built IN939 samples (error bars represent 95% CI).

Sample		Image J						Archimedes' principle	
		Average Porosity (%)		Average Pores/mm²		Average Feret Size (µm)		Relative Density (%)	
1	1A	0.99	**0.93 ± 0.63**	7.14	**6.45 ± 1.50**	31.07	**31.98 ± 11.42**	98.37	**98.65 ± 0.15**
	1B	1.15		6.02		36.96		98.58	
	1C	0.65		6.20		27.90		99.00	
2	2A	0.03	**0.05 ± 0.05**	3.44	**5.09 ± 6.79**	9.97	**11.09 ± 4.38**	99.25	**99.29 ± 0.20**
	2B	0.05		8.24		10.17		99.29	
	2C	0.07		3.58		13.12		99.33	
3	3A	0.12	**0.20 ± 0.26**	5.77	**6.14 ± 2.11**	16.08	**19.42 ± 15.24**	98.81	**98,75 ± 0.19**
	3B	0.32		5.54		26.50		98.67	
	3C	0.15		7.11		15.68		98.76	

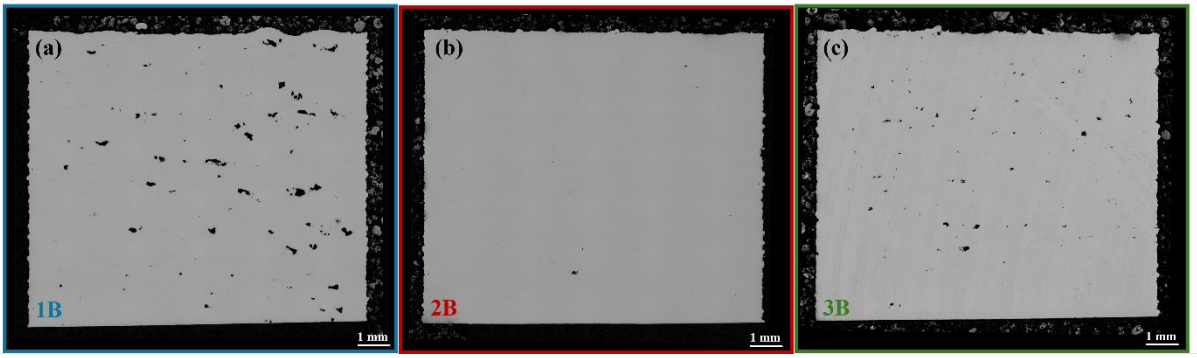

Fig. 4. The as-polished optical micrographs of as-built samples in the XZ plane (parallel to the build direction).

3.4. Microstructure and microhardness

Despite the use of a constant VED, the microstructure of the as-built samples was strongly influenced by the scanning parameters. Optical micrographs and EBSD maps revealed a predominantly columnar grain morphology, with arch-shaped melt pools aligned along the build direction in all samples. The area-weighted average grain sizes were 29.5 ± 8.7 µm, 31.9 ± 9.4 µm, and 36.7 ± 8.9 µm for Samples 1, 2, and 3, respectively. Sample 1 exhibited the highest normalized temperature (Fig. 2(a)) due to its narrow hatch distance, which promoted intense local heat accumulation; however, the combination of high temperature and high scanning speed led to melt pool instability and the formation of large, irregular lack-of-fusion pores [19]. In contrast, Sample 3 showed a lower overall temperature but a highly heterogeneous and non-uniform grain structure, as confirmed by EBSD maps, resulting from the combination of wide hatch distance and low scanning speed that caused uneven heat distribution and inconsistent melting. These observations, supported by 3D thermography, demonstrated that maintaining a constant VED was insufficient to ensure microstructural homogeneity, as process parameters governs the thermal history, melt pool stability, and grain evolution in IN939.

The microhardness values showed only a slight decrease from Sample 1 to Sample 3 (360.1 ± 10.5 HV1, 359.8 ± 16.3 HV1, and 356.7 ± 14.3 HV1, respectively), indicating that strengthening was not governed solely by grain size effects. Despite the progressive increase in average grain size, EBSD-derived parameters revealed a gradual reduction in grain orientation spread (GOS) and kernel average misorientation (KAM). Sample 1 exhibited the highest GOS and KAM values, indicating stronger intragranular lattice distortion caused by steep thermal gradients and unstable melt pool behavior. In contrast, Sample 3 showed lower average misorientation values, suggesting partial relaxation of internal strains through dislocation rearrangement and early-stage recovery, despite the presence of locally heterogeneous deformation [19,22].

The inverse pole figures (IPFs) with respect to the build direction (BD) obtained from the XZ planes in the as-built samples are displayed in Fig. 6. Although nickel-based superalloys typically promote preferential <001> growth due to their cubic crystal symmetry and alignment with the maximum thermal gradient, the IPFs of the as-built samples showed only weak texture development. Sample 1 exhibits a largely random orientation distribution, whereas a gradual decrease in scanning speed and increase in hatch distance in Samples 2C and 3C leads to a slight intensification of <001>//BD and <111>//BD components, as indicated by higher (multiples of random distribution) MRD intensities. This behavior is primarily attributed to the continuously varying thermal gradients generated during the PBF-LB process as a result of the 67° scan rotation. The frequent changes in heat flow direction prevent the establishment of a stable solidification gradient, thereby limiting strong texture development and promoting grain reorientation [23].

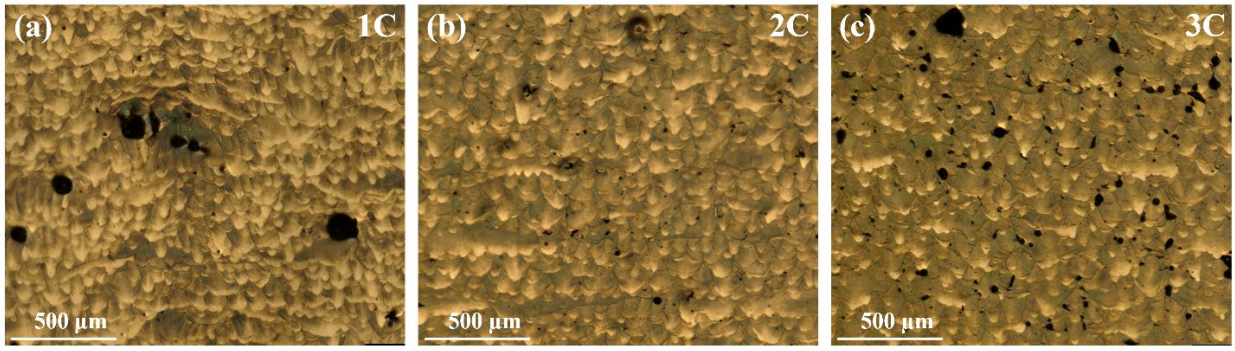

Fig. 5. Optical micrographs of the as-built samples: (a) Sample 1C, (b) Sample 2C and (c) Sample 3C.

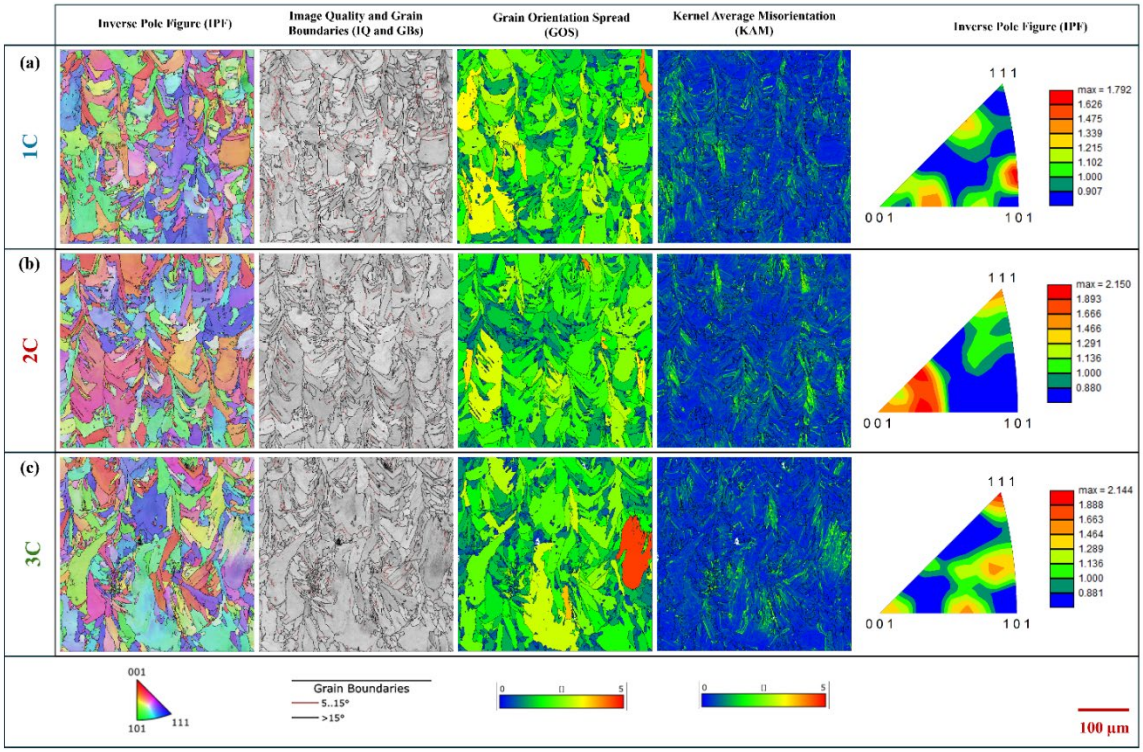

Fig. 6. EBSD maps and inverse pole figures (IPFs) of the XZ planes of the as-built samples: (a) Sample 1C, (b) Sample 2C and (c) Sample 3C.

4. Conclusion

This study systematically investigated the influence of scanning speed and hatch distance combinations at constant VED on the thermal behavior, surface quality, defect formation, and microstructural evolution of IN939 fabricated by the PBF-LB.

- In-situ infrared monitoring revealed that the narrowest hatch distance combined with the highest scanning speed (Sample 1) resulted in the highest normalized temperatures and pronounced heat accumulation, whereas wider hatch distances promoted lower and more stable thermal distributions during the build.
- The intermediate parameter set (Sample 2) exhibited the most favorable combination of properties, achieving the highest relative density (99.29%) and the lowest surface roughness values, indicating a more stable melt pool and effective thermal dissipation.
- Both the narrowest and widest hatch spacing conditions led to increased porosity, with Sample 1 dominated by large LoF defects and Sample 3 primarily containing gas pores and keyhole-related pores.

- EBSD analysis showed a progressive increase in area-weighted average grain size from 29.5 ± 8.7 μm (Sample 1) to 36.7 ± 8.9 μm (Sample 3) with increasing hatch distance.
- Crystallographic texture remained generally weak across all samples, with only a slight intensification of <001>//BD and <111>//BD components observed at lower scanning speeds and larger hatch distances.
- Microhardness values showed minimal variation among the samples, ranging from 356.7 ± 14.3 HV1 to 360.1 ± 10.5 HV1, suggesting that mechanical strengthening was governed primarily by defect formation and matrix characteristics rather than grain size effects alone.

Overall, the results demonstrated that VED alone is not sufficient for the PBF-LB process, as different parameter combinations can produce the same VED but result in significantly different material properties.

References

[1] A. Mostafaei, R. Ghiaasiaan, I.T. Ho, S. Strayer, K.C. Chang, N. Shamsaei, S. Shao, S. Paul, A.C. Yeh, S. Tin, A.C. To, Additive manufacturing of nickel-based superalloys: A state-of-the-art review on process-structure-defect-property relationship, Progress in Materials Science 136 (2023) 101108. https://doi.org/10.1016/j.pmatsci.2023.101108.

[2] M. Shahwaz, P. Nath, I. Sen, Recent advances in additive manufacturing technologies for Ni-Based Inconel superalloys – A comprehensive review, Journal of Alloys and Compounds 1010 (2025) 177654. https://doi.org/10.1016/j.jallcom.2024.177654.

[3] T. Zou, M. Liu, Y. Cai, Q. Wang, Y. Jiang, Y. Wang, Z. Gao, Y. Pei, H. Zhang, Y. Liu, Q. Wang, Effect of temperature on tensile behavior, fracture morphology, and deformation mechanisms of Nickel-based additive manufacturing 939 superalloy, Journal of Alloys and Compounds 959 (2023) 170559.

[4] M.R. Jahangiri, M. Abedini, Effect of long time service exposure on microstructure and mechanical properties of gas turbine vanes made of IN939 alloy, Materials and Design 64 (2014) 588–600. https://doi.org/10.1016/j.matdes.2014.08.035.

[5] B. Zhang, H. Ding, A.C. Meng, S. Nemati, S. Guo, W.J. Meng, Crack reduction in Inconel 939 with Si addition processed by laser powder bed fusion additive manufacturing, Additive Manufacturing 72 (2023). https://doi.org/10.1016/j.addma.2023.103623.

[6] M. Malý, K. Nopová, L. Klakurková, O. Adam, L. Pantělejev, D. Koutný, Effect of Preheating on the Residual Stress and Material Properties of Inconel 939 Processed by Laser Powder Bed Fusion, Materials 15 (2022) 6360. https://doi.org/10.3390/ma15186360.

[7] T. Zou, M. Liu, Q. Wang, Y. Jiang, H. Wu, Z. Gao, Evolutionary mechanisms in the plastic deformation of γ'-Ni 3(Al, Ti)-strengthened additively manufactured nickel-based 939 superalloys at intermediate temperatures, Materials & Design 239 (2024) 112795.

[8] I. Rodríguez-Barber, A.M. Fernández-Blanco, I. Unanue-Arruti, I. Madariaga-Rodríguez, S. Milenkovic, M.T. Pérez-Prado, Laser powder bed fusion of the Ni superalloy Inconel 939 using pulsed wave emission, Materials Science and Engineering: A 870 (2023). https://doi.org/10.1016/j.msea.2023.144864.

[9] W. Abd-Elaziem, S. Elkatatny, T.A. Sebaey, M.A. Darwish, M.A. Abd El-Baky, A. Hamada, Machine learning for advancing laser powder bed fusion of stainless steel, Journal of Materials Research and Technology 30 (2024) 4986–5016. https://doi.org/10.1016/j.jmrt.2024.04.130.

[10] S. Fatemeh, A. Farshidianfar, H. Dalir, Comprehensive review: Advancements in modeling geometrical and mechanical characteristics of laser powder bed fusion process, Optics and Laser Technology 180 (2025) 111480. https://doi.org/https://doi.org/10.1016/j.optlastec.2024.111480.

[11] M.N. Doğu, M.A. Obeidi, H. Gu, C. Teng, D. Brabazon, Powder Bed Fusion–Laser Beam of IN939: The Effect of Process Parameters on the Relative Density, Defect Formation, Surface Roughness and Microstructure, Materials 17 (2024). https://doi.org/10.3390/ma17133324.

[12] G. Marchese, S. Parizia, A. Saboori, D. Manfredi, M. Lombardi, P. Fino, D. Ugues, S. Biamino, The influence of the process parameters on the densification and microstructure development of laser powder bed fused inconel 939, Metals 10 (2020) 1–19. https://doi.org/10.3390/met10070882.

[13] G. Dursun, A. Orhangul, A. Urkmez, G. Akbulut, Understanding the Parameter Effects on Densification and Single Track Formation of Laser Powder Bed Fusion Inconel 939, in: Procedia CIRP, Elsevier B.V., 2022: pp. 258–263. https://doi.org/10.1016/j.procir.2022.03.045.

[14] M.N. Doğu, A. Mussatto, M.A. Yalçın, S. Ozer, K. Davut, M.A. Obeidi, A. Kumar, S. Hudson, D. O'Neill, R. O'Connor, H. Gu, D. Brabazon, A comprehensive characterization of the effect of spatter powder on IN939 parts fabricated by laser powder bed fusion, Materials and Design 235 (2023). https://doi.org/10.1016/j.matdes.2023.112406.

[15] ASTM B311-17, Standard Test Method for Density of Powder Metallurgy (PM) Materials Containing Less Than Two Percent Porosity, (n.d.). https://doi.org/10.1520/B0311-17.

[16] ASTM International, Standard Test Method for Microindentation Hardness of Materials - ASTM E384 - 17, 2017.

[17] M.C.C. Monu, E.J. Ekoi, C. Hughes, S. Sujith Kumar, D. Brabazon, Resultant physical properties of as-built nitinol processed at specific volumetric energy densities and correlation with in-situ melt pool temperatures, Journal of Materials Research and Technology 21 (2022) 2757–2777. https://doi.org/10.1016/j.jmrt.2022.10.073.

[18] A. Mussatto, R. Groarke, R.K. Vijayaraghavan, C. Hughes, P.J. Mcnally, Y. Delaure, D. Brabazon, Assessing dependency of part properties on the printing location in laser-powder bed fusion metal additive manufacturing, Materials Today Communications 30 (2022). https://doi.org/10.1016/j.mtcomm.2022.103209.

[19] M.N. Doğu, Additive Manufacturing of Nickel-Base Superalloy IN939 by Powder Bed Fusion-Laser Beam, n.d.

[20] M.N. Doğu, M.A. Obeidi, H. Gu, C. Teng, D. Brabazon, Powder Bed Fusion–Laser Beam of IN939: The Effect of Process Parameters on the Relative Density, Defect Formation, Surface Roughness and Microstructure, Materials 17 (2024). https://doi.org/10.3390/ma17133324.

[21] M.N. Doğu, S. Ozer, M.A. Yalçın, K. Davut, G.M. Bilgin, M.A. Obeidi, H. Brodin, H. Gu, D. Brabazon, Effect of solution heat treatment on the microstructure and crystallographic texture of IN939 fabricated by powder bed fusion-laser beam, Journal of Materials Research and Technology 24 (2023). https://doi.org/https://doi.org/10.1016/j.jmrt.2023.05.152.

[22] S. Ozer, M.N. Doğu, C. Ozdemirel, G.M. Bilgin, M. Gunes, K. Davut, H. Gu, D. Brabazon, Effect of aging treatment on the microstructure, cracking type and crystallographic texture of IN939 fabricated by powder bed fusion-laser beam, Journal of Materials Research and Technology 33 (2024) 574–588. https://doi.org/10.1016/j.jmrt.2024.09.106.

[23] M.N. Doğu, S. Ozer, M.A. Yalçın, K. Davut, M.A. Obeidi, C. Simsir, H. Gu, C. Teng, D. Brabazon, A comprehensive study of the effect of scanning strategy on IN939 fabricated by powder bed fusion-laser beam, Journal of Materials Research and Technology 33 (2024) 5457–5481. https://doi.org/10.1016/j.jmrt.2024.10.171.